International Journal of Basic and Applied Sciences, 14 (4) (2025) 648-660

International Journal of Basic and Applied Sciences

Website: www.sciencepubco.com/index.php/IJBAS
https://doi.org/10.14419/8psp9843
Research paper

Enhanced Wavelet Block Shrinkage Technique For Mammogram Denoising Using K-Means Clustering And Neural Networks

Ashok Kumar Sahoo [1] *, Rajkumar Rajavel [2]

[1] *Research Scholar, School of Computer Science and Engineering, Christ University, Bangalore, India*
[2] *Associate Professor, Department of AI, ML and Data Science, Christ University, Bangalore, India*
**Corresponding author E-mail: ashok.sahoo123@gmail.com*

Received: July 6, 2025, Accepted: August 17, 2025, Published: August 25, 2025

Abstract

The proposed research study introduces a novel approach for denoising digital mammograms by improving the existing wavelet block shrinkage filtering method with K-Means clustering and a convolutional neural network. This approach involves decomposing both the original and noisy mammograms into frequency subbands using 2D discrete wavelet transformation. The resulting subbands are then grouped into multiple clusters based on similar features of the wavelet coefficients, employing K-Means clustering. This represents an improvement over the traditional block shrinkage method, which uses fixed-size blocks. These clusters from the original and noisy mammograms are paired to train a convolutional neural network, which serves as an optimal shrinkage function. This neural network-based thresholding mechanism replaces traditional hard and soft thresholding methods that rely on a universal threshold. Test results demonstrate that the proposed enhanced wavelet block shrinkage mechanism achieves a 20% improvement in peak signal-to-noise ratio and a 5% increase in structural similarity index score compared to traditional wavelet block shrinkage.

Keywords: *Enhanced Wavelet Block Shrink, Wavelet Shrinkage, K-Means Clustering, Convolutional Neural Network, Digital Mammogram Denoising, Breast Cancer*

1. Introduction

Breast cancer remains one of the most significant causes of mortality among women globally. According to research published by Bray et al. (2024 [1] in the International Agency for Research on Cancer (IARC) journal, 11.6% of all diagnosed cancer cases worldwide in 2022 were related to female breast cancer, making it the most frequently diagnosed cancer among women. National and global statistics from authoritative sources such as the American Cancer Society, Cancer Research UK, and the SEER program in the USA consistently highlight the critical importance of early detection in the successful treatment of breast cancer. Early-stage diagnosis (stage 0 or I) is associated with survival rates of 99% or higher, as noted in studies by Kuroishi et al., 1992 [2] and Chen et al., 2014 [3]. Recent research by Aristokli et al., 2022 [4], Jung et al., 2019 [5], and current breast cancer diagnostic trends underscore that digital mammography is among the most effective imaging techniques for early breast cancer detection. It generally offers a sensitivity of about 78%, aiding significantly in identifying cancer at stages when treatment outcomes are most favorable. This collective evidence reinforces the pivotal role of digital mammography in improving breast cancer prognosis through timely and accurate diagnosis.

1.1 Impact of noisy mammograms on radiologists

Mammograms are often contaminated with noise due to various reasons, including technical, procedural, and patient-related factors. Noise refers to anything that interferes with the accurate interpretation of mammograms, which can lead to false positives, false negatives, or indecision. Attributes such as fine microcalcifications and low-contrast lesions in mammograms are critical for the early identification of breast cancer, as per Warren et al., 2012 [6]. However, the presence of noise in mammograms obscures these attributes. Electronic noise introduces grainy patterns that mimic pathological structures, leading to false positives, as highlighted by Huda et al. (2006 [7] in their research. Dead pixels in the detector of the imaging device create artificial structures that can mislead radiologists into interpreting them as lesions, as per Iflaq et al., 2025 [8]. Therefore, reducing noise in digital mammograms is essential for improving diagnostic accuracy.

1.2 Noise reduction in mammograms

Noise reduction methods can be broadly categorized into procedural (acquisition-based) and scientific (post-processing and algorithmic) approaches. Usage of a high X-ray dose is one of the procedural methods to reduce quantum noise, which is a common type of noise found in mammograms, as highlighted by Saunders et al., 2007 [9]; however, high doses can negatively impact the human body, as warned by Pereira et al., 2021 [10] in their research. Other procedural improvements to noise reduction include automatic exposure control to ensure consistent exposure across different breast densities, improved detector technology with higher detective quantum efficiency, and anti-scatter grids to reduce scatter-induced noise. Although procedural methods aim to minimize noise during image acquisition by optimizing hardware and imaging protocols, they face several inherent limitations. These include a trade-off between noise reduction and radiation dose, constraints in detector technology (i.e., upgrading detectors is costly and may not eliminate quantum noise), and limited adaptability to varied breast densities, among other challenges, as highlighted by Cahn et al., 1999 [11] and da Costa et al., 2019 [12]. Hence, post-processing techniques are often necessary to compensate for these limitations. The traditional post-processing denoising methods rely on mathematical and statistical approaches to suppress noise while preserving critical structures (e.g., microcalcifications, masses). The most effective traditional filtering techniques used in mammography are spatial domain filters, which operate directly on pixel values in the image, and frequency domain filters, which transform the image into frequency components (e.g., Fourier, Wavelet) to separate noise. These methods are less computationally intensive and easy to explain, but they do not achieve the desired improvement in image quality as measured by PSNR (Peak Signal-to-Noise Ratio) and SSIM (Structural Similarity Index Measure) metrics. Hence, there is a growing trend among researchers and the healthcare industry to apply deep learning methods to improve diagnostic image quality. Application of architecture like deep convolution network, encoder-decoder, transformers, and generative adversarial networks has been explored to improve existing denoising techniques of medical images according to recent surveys (Nazir et al., 2024 [13]).

1.3 Our contribution

Frequency-domain wavelet shrinkage is the most common post-processing denoising technique in medical imaging. Wavelet Block Shrinkage (WBS), originally proposed by Cai and Silverman in the early 2000s (Cai & Silverman, 2001 [14]), improves upon classical wavelet shrinkage by grouping neighboring wavelet coefficients (blocks) and thresholding them collectively. Although WBS has shown promising results in noise filtering compared to traditional wavelet shrinkage methods, it still suffers from limitations such as excessive smoothing, inability to adapt to local texture, block size sensitivity, fixed thresholds, and ineffectiveness in filtering non-Gaussian noise (Dewangan et al., 2012 [15]). These shortcomings motivate our research to further improve WBS, ultimately enhancing radiologists' efficiency in detecting breast cancer. In this research, we propose a hybrid approach that integrates the WBS method with AI-driven techniques such as K-Means clustering and convolutional neural networks (CNN) to further enhance block shrinkage. Since WBS applies thresholding to blocks or groups of coefficients rather than to individual coefficients, its efficiency heavily depends on selecting an optimal block size. Therefore, in this experiment, the block mechanism is enhanced by using K-Means clustering to group similar coefficients or patches based on feature similarities such as texture, magnitude, and local variance, before applying shrinkage to these clusters. This study further establishes that the threshold value used for shrinkage in WBS is critical; depending on this value, a block is either preserved (indicating it primarily contains signal) or discarded (indicating it primarily contains noise). Accordingly, we replace traditional thresholding methods in WBS with an adaptive, content-aware CNN-based shrinkage function capable of generalizing noise pattern detection across different noise types and varying noise levels (σ) in mammograms collected from machines of different manufacturers. The CNN architecture, acting as the shrinkage function, is carefully designed to maintain optimal computational resource requirements. Experimental results demonstrate that the proposed Enhanced Wavelet Block Shrinkage (EWBS) method achieves superior PSNR and SSIM metrics compared to traditional wavelet shrinkage techniques.

2. Methods

2.1 Type of noise in mammograms

Mammograms can be contaminated with quantum noise (also known as photon noise), electronic noise, and fixed pattern noise resulting from anomalies in the imaging device, such as suboptimal detector function or statistical variations in X-ray photon absorption. Procedural inaccuracies—including poor calibration, grid misalignment, inadequate compression, improper positioning, and low radiation dose—also contribute to noise in mammograms. Patient-related factors such as body movement, high breast density, and implants further cause noise. These noise components in mammograms can be modeled using the Poisson noise model, the Gaussian noise model, the Salt-and-Pepper noise model, or the Speckle noise model, as per multiple studies by Zhang et al., 2010 [16], Rahman et al., 2022 [17], and Perez et al., 2024 [18].

2.1.1 Poisson noise

Quantum spot noise can be represented by the Poisson noise model and is proportional to the mean signal intensity. It arises from the inherent randomness of X-ray interactions with breast tissue, causing random fluctuations in pixel intensity and follows a Poisson distribution, as highlighted by Kumar et al., 2022 [19]. Poisson noise obscures subtle features like microcalcifications. The probability $P(x)$ of detecting x photons at a specific image location is given by the Poisson distribution as specified in equation (1).

$$P(x) = (\lambda^x * e^{-\lambda})/x! \quad (1)$$

Where λ (lambda) represents the average number of X-ray photons expected to be detected at that location.

2.1.2 Gaussian noise

Noise arising from electronic circuit noise in the scanner, sensor noise, and analog-to-digital conversion errors can be formulated using the Gaussian noise model, as stated by Ghazdali et al. (2024 [20] in their research. This noise corrupts the mammogram by causing random variations in pixel intensity across the image, which can blur the mammogram and minimize the contrast, making it difficult to differentiate between subtle features and real tissue structures. High levels of Gaussian noise can significantly degrade image quality and potentially

obscure suspicious lesions. A general image degradation model $g(x, y)$can be used to represent a perfect noise-free corupted by $f(x, y)$being corruptedby noise $n(x, y)$during acquisition as expressed in equation (2).

$$g(x, y) = f(x, y) + n(x, y)$$

2.1.3 Salt-and-Pepper noise

Unexpected variations in image signal intensity, dust particles in the image acquisition system, faulty electronic components, transmission errors, and similar factors induce noise that can be modeled by the Salt-and-Pepper noise model. This noise type does not represent a statistical distribution of photons according to the study done by Pashaei et al., 2023 [21]. Instead, random bright (white) and dark (black) pixels are scattered across the mammogram when this noise occurs, resembling salt and pepper granules. These granules can either mimic microcalcifications—a potential sign of cancer—or obscure them if present. The probability of a pixel being corrupted by salt-and-pepper can be denoted by P_s for salt (white) and P_p for pepper (black). A probabilistic model is used to mathematically describe the likelihood of a pixel being corrupted. Let an original noise-free image have pixel intensity $I(x, y)$. The salt-and-pepper noise is represented by a random variable $N(x, y)$ that can take on three values:

$(a)\ N(x, y) = 1\ with probability\ P_s\ represents$
$a\ white\ pixel\ caused\ by\ salt\ noise;$
$(b)\ N(x, y) = 0\ with probability\ P_p\ represents$
$a\ black\ pixel\ caused\ by\ pepper\ noise;$
$(c)\ N(x, y) = I(x, y)\ with probability\ 1 - (P_s + P_p)$
$represents the\ original\ pixel\ intensity$
$remaining\ unchanged;$

The corrupted image intensity $g(x, y)$ can be represented as given in equation (3)

$$g(x, y) = I(x, y) * \big(1 - N(x, y)\big) + N(x, y)$$

2.1.4 Speckle noise

Speckle noise arises from the coherent nature of the imaging wave used in mammography and is granular in pattern. This noise originates from the constructive and destructive interference of scattered waves reflecting from tissue structures with varying phases. Unlike Gaussian noise, speckle noise is multiplicative in nature, meaning that it varies in proportion to the image intensity, which complicates its removal during image processing. In mammograms, speckle noise creates a mottled texture that reduces image contrast and obscures fine structural details, thus hindering accurate lesion detection and analysis.

2.2 Conventional mammogram denoising methods

Radiologists' detection accuracy and subsequent diagnosis are significantly affected by the types of noise present in mammograms. Cederstrom et al., 2014 [22] explored how quantum noise and anatomical noise can hinder the detection of small microcalcifications and masses and advised reconsidering beam-quality optimization to achieve better mammogram quality. Chowdappa & Sheshadri, 2018 [23], in their research, highlighted the importance of noise reduction in medical image analysis, demonstrating that it directly impacts clinical decision-making and patient outcomes. Their findings further underscore the vital importance of probabilistic, data-driven noise characterization in medical imaging. Therefore, optimal noise filtering techniques are essential in mammograms to ensure that microcalcifications, masses, or other lesions are not distorted.

Diagnostic image denoising methods can be broadly categorized as linear filtering and nonlinear filtering. Linear filtering applies a fixed filtering function uniformly across the mammogram. One such method, the linear adaptive filtering technique, is available in both the spatial and frequency domains and includes algorithms such as least mean squares (LMS), recursive least squares (RLS), and the adaptive noise-canceling method. The LMS algorithm regulates the filter constants to optimize the mean square error between the anticipated signal and the actual output, offering simplicity and ease of implementation. However, its convergence speed can be slow and is sensitive to the step size parameter. The RLS algorithm, although it has fast convergence and robustness due to its mechanism for continuously updating the filter coefficients to minimize the sum of squared differences between actual and expected signals, is not commonly used in practice because of its computationally intensive nature. While linear adaptive methods are good at preserving edges, their tendency to oversmooth can hide critical small features, such as microcalcifications, highlighted by Arias-Castro et al., 2006 [24].

In contrast to linear adaptive filtering, nonlinear filtering techniques use nonlinear functions—meaning their outputs are not linear combinations of input values—to filter noisy mammograms and are more effective at preserving edges and granular details. Nonlinear techniques include Median Filtering, Anisotropic Diffusion, and Wavelet Thresholding (Bhateja et al. [25]). Wavelet threshold denoising is a powerful image denoising technique: it first transforms the image to the wavelet domain using the Discrete Wavelet Transform (DWT), shrinks small coefficients (which are likely noise), and then reconstructs the image using the inverse DWT (IDWT). Each of these nonlinear filtering techniques has its own set of limitations and trade-offs, but they share common adaptive challenges due to inconsistent performance across different breast tissue types as per the exploration done by Warren et al., 2012 [6], and Carnahan et al., 2023 [26].

2.3 Wavelet-based denoising of mammograms

Wavelet shrinkage is a powerful technique for denoising mammograms, particularly effective against Poisson and Gaussian noise.

2.3.1 Wavelet function

In the first step, the mammogram image $f(x,y)$ is transformed into the wavelet domain. This decomposition breaks down the mammogram into different subbands that represent spatial and frequency information. Various wavelet functions ψ(x) can be used to perform the decomposition at multiple levels. The Wavelet function can be mathematically represented as shown in the following equation (4).

$$Wi,j = \int Z\, f(x,y) * \psi(x - i_a, y - j_b)\, dx\, dy$$

Where $W_{i,j}$ represents the wavelet coefficient at scale i and orientation j, a denotes the scaling parameter, b represents the shifting attribute, and ψ(x) denotes the chosen wavelet function.

2.3.2 Wavelet shrinkage

In the second step, the wavelet coefficients of each subband are compared against their respective threshold value λ. Coefficients below the threshold are considered dominated by noise and are shrunk toward zero, while coefficients above the threshold are assumed to contain significant image information and are kept relatively unchanged. This step is known as thresholding, and different functions can be applied for this purpose. A common choice is the "soft thresholding" function:

$$shrink(W_{i,j}) = sign(W_{i,j}) * \max(|W_{i,j}| - \lambda, 0)$$

Where $sign(W_{i,j})$ preserves the sign of the coefficient, and λ denotes the threshold value. Hard thresholding is a simpler alternative to soft thresholding. If the absolute value of the wavelet coefficient is below the threshold ($|W_{i,j}| < \lambda$), the coefficient is considered dominated by noise and is set to zero. This effectively removes the noisy coefficient from the reconstruction process and can be represented mathematically as in equation (5).

$$h(W_{i,j}) = \{$$
$$W_{i,j}\ if\ |W_{i,j}| \geq \lambda$$
$$0\ if\ |W_{i,j}| < \lambda$$
$$\}$$

Where $h(W_{i,j})$ represents the thresholded coefficient.

2.3.3 Inverse Wavelet Transform

In the third and final step, the modified coefficients are used to reconstruct a denoised mammogram using the inverse wavelet transform. The noise-free image, $f'(x,y)$, can be obtained by the equation (6).

$$f'(x,y) = \sum\sum W_{i,j} * \psi'(x - i_a, y - j_b)$$

Where ψ′(x) denotes the corresponding scaling function for the chosen wavelet.

2.3.4 Universal threshold

Though the thresholding idea is effective, it is often complex to discover a suitable threshold value. The universal thresholding approach automates the threshold selection process in wavelet shrinkage. It derives a threshold based on the statistical properties of the noise level (σ) and the properties of the wavelet. Here is the equation (7) for the universal threshold in 1D denoising:

$$\lambda = \sigma * \sqrt{\{2 * log(N)\}}$$

Where the noise standard deviation is represented by σ, and N denotes the total number of wavelet coefficients. While convenient, the universal threshold treats all subbands of the decomposed mammogram equally, highlighted by Amiriebrahimabadi et al, 2024 [27]. This approach is problematic because noise characteristics may vary across different subbands (e.g., finer scales might exhibit higher noise levels). A single threshold cannot effectively address this variation, potentially resulting in over-thresholding or under-thresholding in different subbands. For more refined denoising, techniques such as subband-dependent thresholding or data-driven threshold selection methods are explored.

2.4 Block Shrink

Block Shrink, a fully data-driven approach, aims to address noise variations across subbands. Block thresholding processes wavelet coefficients in local groups (blocks) instead of individually. This method ensures that the threshold value closely corresponds to the noise level within each block (Mencattini et al., 2006 [28]). One approach calculates the average coefficient magnitude within a block $|W_{i,j}|$ and compares it to a threshold η_B. Coefficients below a certain proportion η of the average are shrunk towards zero. Here is a simplified equation (8):

$$h(W_{i,j}) = \{$$
$$W_{i,j}\ if\ |W_{i,j}| \geq\ \eta * |W_{i,j}|_{block}$$
$$sign(W_{i,j}) * \max(|W_{i,j}| - \lambda_B, 0)\ if\ \eta * |W_{i,j}|_{block} > |W_{i,j}| \geq \lambda_B$$
$$0\ if\ |W_{i,j}| < \lambda_B$$
$$\}$$

Where $h(W_{i,j})$ denotes the threshold coefficient, $W_{i,j}$ represents the original wavelet coefficient, $|W_{i,j}|_{block}$ is the average magnitude within the block, η is a shrinkage parameter ($0 < \eta < 1$), and λ_B denotes the base threshold for the block.

The block thresholding approach improves estimation accuracy by leveraging the dependencies among neighboring wavelet coefficients. It exploits the strengths of both SureShrink and NeighShrink while discarding their respective weaknesses. WBS adapts the threshold settings of each wavelet subband using Stein's Unbiased Risk Estimate (SURE) minimization. Although block thresholding offers advantages over universal thresholding, the careful selection of parameters—specifically the shrinkage parameter, η, and the base threshold, λ_B—as well as optimization of block size, is crucial for effective noise removal. The choice of block size is especially important: large blocks may fail to capture local noise variations, whereas very small blocks can be computationally expensive and prone to noise sensitivity, as per, Cai & Silverman, 2001 [14]. While a suboptimal block size can cause visual artifacts at block boundaries and inconsistent texture in otherwise smooth tissue regions, Vikhe et al., 2019 [29] highlighted the importance of adaptive thresholding for effective denoising and contrast enhancement in Wavelet Block Shrinkage (WBS). Dewangan et al., 2012 [15] demonstrated that adaptive wavelet thresholding functions in block shrinkage provide improved image denoising performance under different noise conditions. These studies conclude that, alongside optimal block size, an efficient thresholding function adaptive to different noise types and levels is pivotal for WBS. This forms motivation for the current research.

2.5 Deep learning for denoising mammograms

To address the shortcomings of conventional spatial and frequency domain filtering, many researchers are currently exploring the use of Artificial Intelligence (AI), especially deep learning methods, for denoising mammograms. Recent advancements in computing, particularly GPU-based processing and storage technologies, have enabled researchers to store and train complex machine learning algorithms using massive amounts of diagnostic image data. Nazir et al. (2024 [13] identified in their survey that 40% of current research on denoising explores applying deep convolutional networks (DCNN) for filtering noise from medical images. Variants like DnCNN (Denoising Convolutional Neural Network) use residual learning for efficient and generalizable denoising. These CNN-based denoising methods are effective at preserving edges and fine details while reducing noise. However, they have limitations when dealing with unseen noise types.

Eckert et al., 2019 [30] proposed a physics-driven data augmentation technique to train a CNN based on a deep residual network architecture. This method operates on noise maps of images, aiming to directly learn and remove the noise component. Combining physics-based augmentation with the CNN architecture enables effective denoising of images corrupted by both real and simulated noise. However, the method relies on careful preprocessing (noise transformation and augmentation) for optimal performance, which may require domain expertise and additional processing steps.

Singh et al., 2019 [31] explored a CNN architecture based on U-Net/Encoder-Decoder networks capable of capturing both global context (through downsampling/encoding) and reconstructing the image using upsampling/decoding. While effective at extracting fine textures and preserving anatomical details compared to classical methods, these models require large, well-annotated datasets of clean/noisy image pairs for training. Their performance drops with insufficient or unrepresentative data.

Ghosh et al., 2020 [32] used a Deep Convolutional Denoising Autoencoder (DDAE) as the primary method for image denoising. The model is structured as an autoencoder with multiple convolutional layers in both the encoder and decoder parts. While effective in noise reduction and preserving critical anatomical details necessary for clinical interpretation, it has the limitation of potentially oversmoothing fine details if not carefully regularized or designed, which can hide subtle pathologies.

Although these modern approaches have shown promising results in filtering noise and preserving details due to their adaptive and data-driven nature, they still face challenges such as loss of diagnostic features, poor generalization, and interpretability issues. Furthermore, the high computing power required for AI-driven denoising entails substantial costs.

2.6 Enhance Wavelet Block Shrink

The proposed EWBS method addresses the challenge of selecting an optimum block size in traditional Wavelet Block Shrinkage (WBS) by leveraging K-Means clustering. Instead of partitioning a wavelet subband into multiple fixed-size blocks of $b1 * b2$, the subband is divided into a predefined number (k) of clusters. These clusters group similar wavelet coefficients within a subband based on features such as energy (sum of squared coefficients), mean, variance, texture, directionality, and softness in the wavelet domain. This enhanced grouping mechanism produces more coherent clusters or patches, to which shrinkage is applied individually. The proposed architecture for K-Means clustering-based block creation is illustrated in Fig. 1. As shown in this diagram, a one-level two-dimensional discrete wavelet transform is applied to mammograms, decomposing them into the frequency subbands LL, LH, HL, and HH. Each subband is represented by a matrix of wavelet coefficients as depicted in Figure 2, and each color group represents a potential K-Means cluster. Fig. 3. shows sample wavelet coefficients of different subband matrices. Further, the conventional hard and soft thresholding functions— which use rule-based thresholds such as the universal threshold (Donoho & Johnstone), SureShrink, VisuShrink, or BayesShrink—are replaced with a data-driven CNN-based shrinkage function. The training architecture of the CNN-based shrinkage function is illustrated in Fig. 7. The CNN-based shrinkage function aims to build a generalized denoiser capable of filtering mammograms acquired from different vendors and contaminated with various types of noise. It is trained using the desired characteristics of each subband cluster pair from the original (Fig. 4) and noisy (Fig. 5) mammograms after 2-D wavelet decomposition. All training mammograms are mixed with three different types of noise—Speckle, Gaussian, and Salt-and-Pepper—at four noise levels (σ= 10, 20, 30, 40) collected from scanners of two different vendors, DBA and HOWTEK. Thus, a total of 50 (original) * 3 (types of noise) * 4 (σ = 10, 20, 30, 40) = 600 mammograms were used to train the CNN. Poisson noise was not considered because of its low probability of occurrence. This EWBS mechanism, based on K-Means clustering and neural network, removes noise in mammograms, as depicted in Fig. 8.

2.6.1 Wavelet Scheme

In this experiment, a two-dimensional one-level wavelet decomposition method used to break down mammograms, generating detail sub-band coefficients in three orientations: horizontal (H), vertical (V), and diagonal (D). This transformation yields a total of four subbands; of these, three subbands (HH, HL, LH), which contain noise elements, are considered for shrinkage, while the LL subband, primarily containing signal, is not. Increasing the number of decomposition levels leads to greater computational complexity. Therefore, the decomposition level is limited to one in this research, enabling the subbands to effectively capture the mammogram's frequency characteristics while maintaining computational feasibility. Each training mammogram image is decomposed twice using two families of wavelet bases, Symlets and Coiflets, chosen as per the recommendation of Benhassine et al., 2021 [33], resulting in $600(noisy\ mammograms) * 2(basis\ family) = 1200$ wavelet-decomposed images to train the CNN.

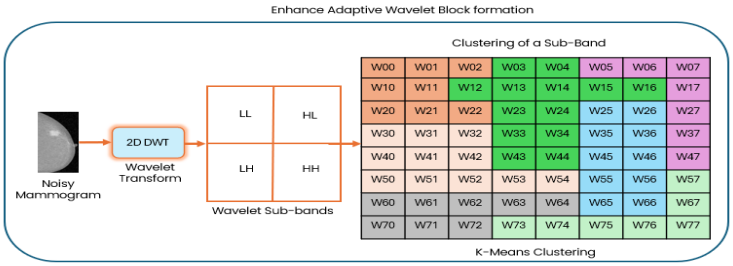

Fig. 1: K-Means clustering-based block creation

W00	W01	W02	W03	W04	W05	W06	W07
W10	W11	W12	W13	W14	W15	W16	W17
W20	W21	W22	W23	W24	W25	W26	W27
W30	W31	W32	W33	W34	W35	W36	W37
W40	W41	W42	W43	W44	W45	W46	W47
W50	W51	W52	W53	W54	W55	W56	W57
W60	W61	W62	W63	W64	W65	W66	W67
W70	W71	W72	W73	W74	W75	W76	W77

Fig. 2: Illustration of K-Means clustering of wavelet coefficients matrix at a subband level

```
LH shape: (2746, 2063) Sample values:
 [[-124.    -0.5   -1.     0.     0. ]
 [   2.    -0.5    0.     0.5    0. ]
 [   0.5    1.    -3.     1.     0. ]
 [  -1.5    0.    -0.5    0.5    0. ]
 [   0.     0.     0.     0.     0. ]]
HL shape: (2746, 2063) Sample values:
 [[127.   -0.5   0.    0.    0. ]
 [ -2.    0.5   0.   -1.5   0. ]
 [  0.5  -1.    3.    1.    0. ]
 [ -1.5   0.   -0.5   0.5   0. ]
 [  0.    0.    0.    0.    0. ]]
HH shape: (2746, 2063) Sample values:
 [[127.   -0.5   0.   -2.    0. ]
 [  2.    1.5   0.    0.5   0. ]
 [ -0.5   1.    3.   -1.    0. ]
 [ -1.5   2.    1.5  -0.5   0. ]
 [  0.    0.    0.    0.    0. ]]
```

Fig.3: Sample wavelet coefficients matrix of LH, HL, and HH subbands

2.6.2 K-Means Clustering

One of the challenges with block shrinking of mammogram wavelet coefficients is the presence of block artifacts, where the boundaries of blocks become visible in the processed mammogram. Do et al., 2002 [34], Pizurica et al., 2006 [35], and Starck et al., 2008 [36] highlighted in their research, this problem arises from suboptimal fixed-size blocks and threshold parameters, which are based on the assumption that the signal within a block is locally correlated and the noise is stationary—that is, its statistical properties (e.g., mean, variance) do not change across the mammogram. These assumptions simplify the thresholding process by allowing a uniform approach to be applied across different blocks. This oversimplification can lead to loss of fine details, poor edge preservation, over-smoothing, or block artifacts during denoising, as the assumption works on the principle, either a block is dominated by noise or by image features. Mammograms often contain non-uniform noise due to varying tissue densities. In our proposed improved block shrinkage method, we address the shortcomings of the local correlation assumption by grouping wavelet coefficients across the mammogram based on homogeneous characteristics of each sub-band—that is, based on the similarity of mean, variance, and smoothness. K-means clustering in the proposed approach creates groups with varying numbers of wavelet coefficients, as shown in Fig. 2, in each subband, based on homogeneity rather than fixed-size $b1 * b2$ blocks. Consequently, the cluster (or block) threshold is more adaptive for each cluster. While Fig. 2 is for representational and illustration purposes, the actual visualization of K-Means clustering of a clean mammogram is shown in Fig. 4, and of a noisy mammogram is shown in Fig. 5. The Silhouette Coefficient method was utilized to determine the optimal number of clusters (k) for K-Means clustering in the enhanced Block Shrink (EWBS) approach. Instead of computing standard K-Means for all possible values of k, this experimen.t employed $MiniBatchKMeans$, hich updates cluster centers in small batches, making it scalable to millions of points. Since silhouette score calculation is computationally intensive ($O(N^2)$), it was computed on a random sample of 10,000 wavelet coefficients to approximate cluster quality. The search for k was performed in two stages: a coarse search, which evaluated a subset of k values to quickly identify a promising range, followed by a refined search around the best coarse result. This method evaluates how well wavelet coefficients are assigned to their

respective clusters and was used to determine an optimal *k* value—2000—which yielded a high average silhouette score, as shown in Fig. 6. A very large *k* was avoided, as it could result in clusters containing only a few pixels, thereby reducing interpretability. This K-Means clustering model was implemented using the Scikit-learn library.

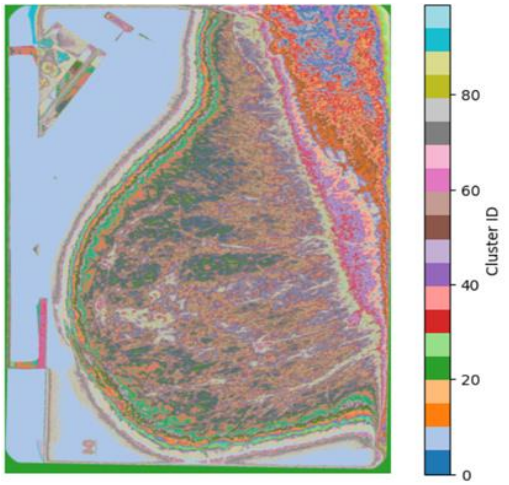

Fig. 4: Visual representation of K-Means Clustering of a clean mammogram

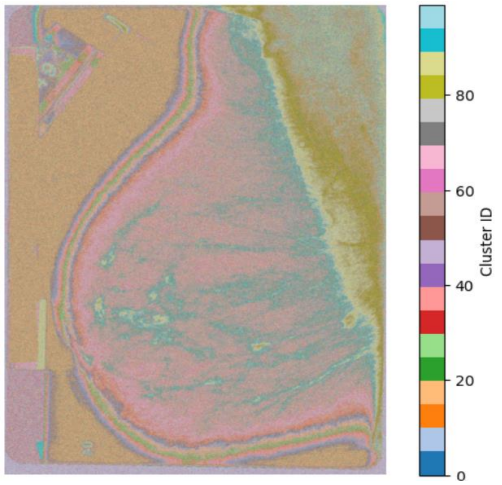

Fig.5: Visual representation of K-Means Clustering of a noisy mammogram

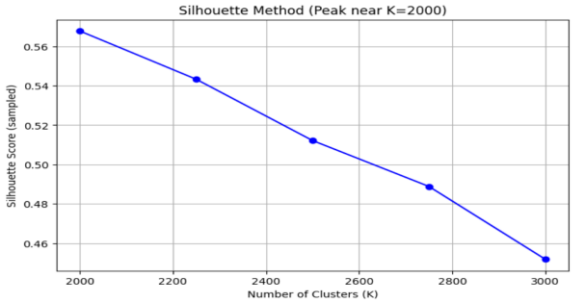

Fig. 6: K value optimization using the Silhouette Method

2.6.3 Convolutional Neural Network (CNN)

In this work, a CNN is employed as a learned shrinkage function in the wavelet domain for the denoising of mammograms. Unlike traditional thresholding techniques, which use manually or statistically determined thresholds that often fail to adapt to the heterogeneous nature of mammographic tissue and noise, the proposed method trains a CNN to directly learn the mapping between noisy and clean wavelet coefficients. The CNN operates on localized subbands—specifically the high-frequency LH, HL, and HH components—capturing subtle textural variations and directional information critical for preserving diagnostic features such as microcalcifications and lesion boundaries. To group semantically or statistically similar regions of wavelet coefficients, K-Means clustering is applied separately to each subband, forming irregularly sized clusters that represent coherent noise structures or texture patterns. Also, location features (x, y) are included alongside coefficients when clustering, to keep the positional information intact. Since CNNs require fixed-size inputs, each irregular cluster is preprocessed into a regular grid by one of the following strategies as appropriate for the 2000 clusters: (i) resizing the coefficient patch using bicubic interpolation, (ii) zero-padding smaller clusters to a fixed size (i.e., 16*16), or (iii) extracting the largest square sub-block from each cluster. This preprocessing ensures that input tensors to the CNN maintain consistent dimensionality while preserving the local statistical characteristics of the original wavelet data. Furthermore, each cluster is normalized (e.g., via min-max or z-score normalization) to mitigate scale variability across clusters and subbands, thereby facilitating stable training. The CNN architecture (Fig. 9) comprises four convolutional layers, a design choice that balances representational capacity with architectural simplicity to avoid overfitting, especially when working with limited or localized wavelet data. The first and second convolutional layers use 3×3 kernels to effectively capture local correlations and edge energy (wavelet coefficient) patterns within each preprocessed block (cluster), while the final layer uses a 1×1 kernel to refine and project the learned features back to the coefficient space with minimal spatial blending. The number of filters ($32 \rightarrow 64 \rightarrow 32 \rightarrow 1$) is selected to allow sufficient feature expansion and compression, enabling the network to extract a rich intermediate representation while keeping the output dimension aligned with the original single-channel wavelet subband. ReLU (Rectified Linear Unit) is used as the activation function after each intermediate layer instead of sigmoid, as ReLU promotes sparsity in activations, speeds up convergence, and avoids vanishing gradient issues—properties that are particularly beneficial when modeling the sparse and directional nature of wavelet coefficients. In contrast, sigmoid saturates quickly and limits gradient flow, which would hinder the model's ability to preserve high-frequency diagnostic content. To preserve the local characteristics of the input clusters throughout the network, padding is set to 1 in all 3×3 convolutions, ensuring that the denoised coefficients align spatially with their original positions. This architectural consistency is essential in the context of wavelet-based reconstruction, where spatial misalignment can distort the final image. Overall, this design facilitates adaptive, data-driven shrinkage that surpasses traditional rule-based thresholding methods by learning context-aware noise suppression while maintaining critical anatomical structures in mammographic imagery.

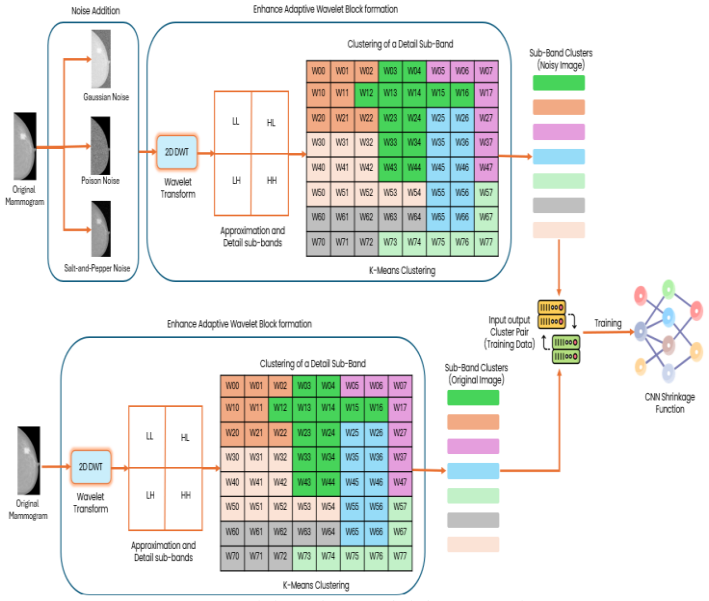

Fig. 7: Training of CNN Shrinkage Function

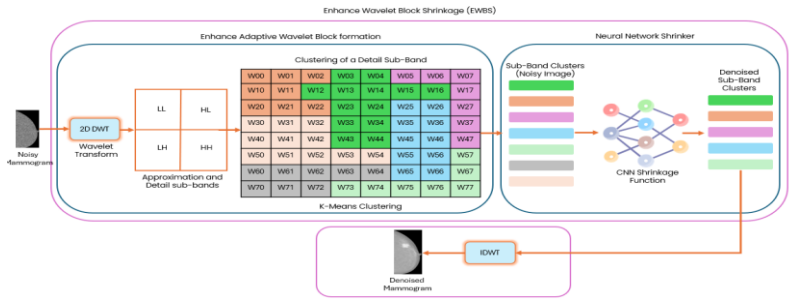

Fig. 8: Denoising the Mammograms using the EWBS

2.6.4 Neural network input data

In this research, the DDSM (Digital Database for Screening Mammography) dataset (Heath et al., 2000 [37]) is used for experimentation. A total of 50 original mammograms, each having a resolution of $1800 * 2300$, considered for training. These mammograms are further combined with three types of noise, four noise levels, and two wavelet basis functions, resulting in $50(original\ mammograms) * 3(types\ of\ noise) * 4(noise\ levels) * 2(wavelet\ basis\ function) = 1200$ decomposed noisy mammograms used to train the CNN. Noisy (feature, Fig. 5) and clean wavelet (target, Fig. 4) coefficient pairs were utilized to train the CNN shrinkage function. Since we apply two-dimensional, one-level, wavelet decomposition, each mammogram transformation produces three subbands, which are further partitioned into 2000 clusters (via K-Means). This process generates $1200 * 3 * 2000 = 7{,}200{,}000$ pairs of data points for training.

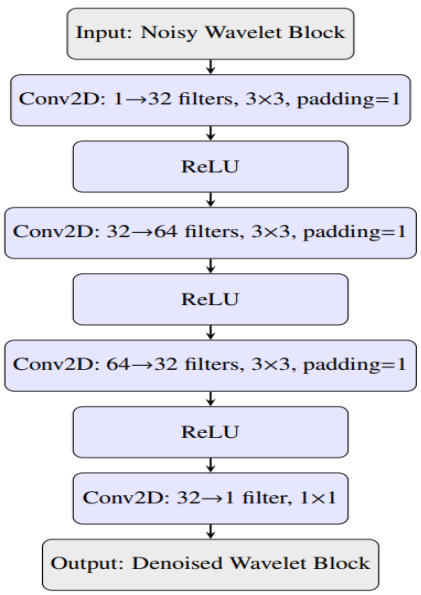

Fig. 9: CNN architecture acting as a shrinkage function in wavelet domain.

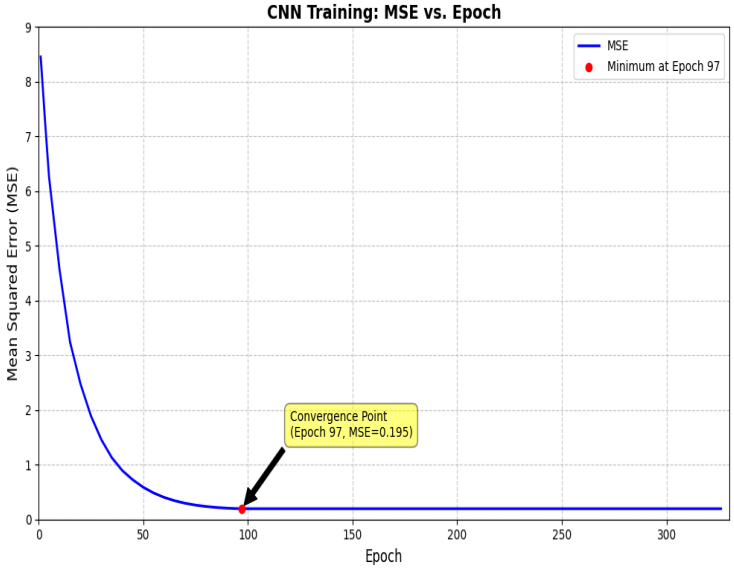

Fig. 10: MSE of validation datasets across 326 Epochs

2.6.5 Training neural network

This research study employed a CNN comprising four convolutional layers and three activation layers (Fig. 9), which facilitated fast training and helped prevent overfitting. The network includes neither pooling nor fully connected layers to preserve the spatial resolution of small wavelet blocks. Input wavelet coefficient clusters were reshaped to $(16 * 16)$ using preprocessing mechanisms such as interpolation and zero-padding. The proposed CNN shrinkage model was trained in a supervised learning framework using 7,200,000 data points generated from paired wavelet coefficient datasets derived from clean and synthetically noised mammographic images as shown in the Fig. 7. The CNN was optimized to model the relationship between noisy wavelet coefficient clusters and their corresponding clean clusters by minimizing the Mean Squared Error (MSE) loss, thereby enabling precise, coefficient-wise denoising in the wavelet domain. The model was implemented with PyTorch and optimized using the Adam optimizer with default parameters $\beta_1 = 0.9, \beta_2 = 0.999$. An initial learning rate of $(1 * 10^{-3})$ was adopted, with cosine annealing applied to gradually reduce the learning rate throughout training. A batch size of 64 was selected to balance memory constraints and statistical efficiency. To avoid overfitting and improve generalization, training utilized early stopping based on validation loss and incorporated coefficient-level augmentations such as random flipping and rotation. Each training epoch included coefficient block pairs sampled from across multiple mammograms, allowing the network to encounter a diverse range of anatomical and noise patterns. The network was trained for up to 326 epochs on an NVIDIA GPU, with convergence achieved around the 97th epoch. This training regime enabled the CNN to learn a nonlinear, subband-specific shrinkage function that outperformed traditional threshold-based methods in both quantitative denoising metrics and visual preservation of diagnostic features such as edges and microcalcifications. Fig. 10 presents the MSE (Mean Squared Error) of the trained CNN across 326 epochs; MSE is initially high due to the random initialization of weights and biases, but gradually reaches a minimum at the 97th epoch and remains stable thereafter.

Table 1: Average PSNR of traditional wavelet thresholding denoising techniques and proposed EWBS for 120 test mammograms (benign, malignant, and negative) added with different levels of Gaussian, Speckle, and Salt-and-Pepper noise.

Level of Gaussian and Speckle noise mixed (σ)	Level of Salt and Pepper prob mixed	PSNR of WBS with universal hard thresholding	PSNR of WBS with VisuShrink soft thresholding	PSNR of Proposed EWBS
10	0.01	24.52	33.72	43.52
20	0.02	22.32	29.75	39.67
30	0.03	21.29	27.67	36.81
40	0.04	20.64	26.35	34.59

Table 2: Average SSIM of traditional wavelet thresholding denoising techniques and proposed EWBS for 120 test mammograms (benign, malignant, and negative) added with different levels of Gaussian, Speckle, and Salt-and-Pepper noise.

Level of Gaussian and Speckle noise mixed (σ)	Level of Salt and Pepper prob mixed	SSIM of WBS with universal hard thresholding	SSIM of WBS with VisuShrink soft thresholding	SSIM of Proposed EWBS
10	0.01	0.889	0.91	0.93
20	0.02	0.880	0.91	0.91
30	0.03	0.871	0.90	0.90
40	0.04	0.863	0.90	0.88

2.6.6 Testing the neural network

The trained CNN is tested on mammograms representing different breast cancer types, namely negative, benign, and malignant, with both calcification and mass lesion types (a total of 5 combinations) to evaluate the efficiency of the proposed denoiser. Two mammograms from each of these five categories are used as test data and corrupted with different types of noise—Gaussian, Speckle, and Salt-and-Pepper—at four different noise levels (σ). This results in a total of 120 noisy mammograms (2 from each category * 5 categories * 3 types of noise * 4 noise levels = 120). These 120 noisy mammograms are denoised using the EWBS mechanism; Fig. 8 illustrates the workflow. The visual test result of the EWBS denoising mechanism is shown for a sample noisy mammogram in Fig. 11. This shows the EWBS's ability to denoise while preserving key features, that is, masses (blue circles) and microcalcifications (red arrows). The proposed EWBS test results on the 120 test images are compared with those of other methods—block shrink with universal hard thresholding and block shrink with VisuShrink soft thresholding. The average PSNR and SSIM results over the various noise types and noise levels for these test mammograms are presented in Tables 1 and 2 and are discussed in detail in the following section.

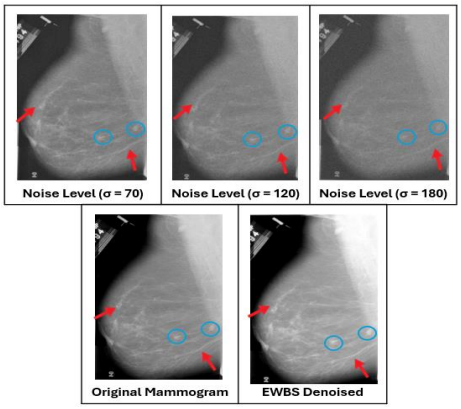

Fig. 11: EWBS denoising test result enhancing masses (circle) and microcalcifications (arrow) in a mammogram

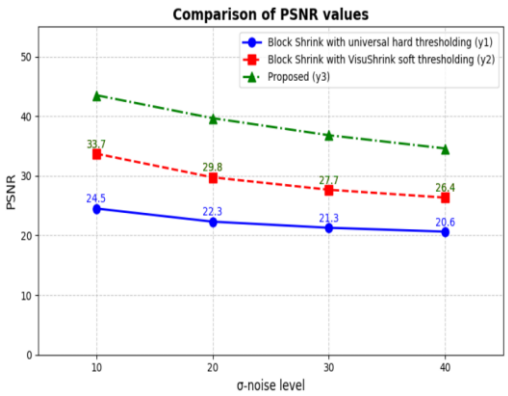

Fig.12: PSNR evaluation of the proposed method with other conventional wavelet shrinkage for several levels of noise

3. Results

The proposed method for denoising mammograms, which integrates a wavelet shrinkage mechanism with K-Means clustering and a CNN, was built and evaluated on DDSM images using Anaconda Distribution 2025.06, on a GPU server, in Christ University HPC lab. The effectiveness of our approach was assessed using peak signal-to-noise ratio (PSNR) and structural similarity index (SSIM) metrics.
The evaluation parameter PSNR measures the quality of a reconstructed signal compared to the original. A higher PSNR value indicates better reconstruction quality. PSNR is calculated in decibels (dB) using equation (9)

$$PSNR = 20 * log10(MAX_{Intensity}/MSE^{0.5})$$

The value of the maximum possible intensity of the image (255 for 8-bit images) is represented by $MAX_{Intensity}$. The Mean Squared Error (MSE) quantifies the average squared difference between corresponding pixels in the original and reconstructed images.
The Structural Similarity Index (SSIM) evaluates the perceived similarity between a reconstructed image and the original by considering luminance, contrast, and structural information. SSIM values range from -1 (completely dissimilar) to 1 (identical), as simplified in equation (10).

$$SSIM = (2\mu_x\mu_y + C_1)(2\sigma_{xy} + C_2)/((\mu_x^2 + \mu_y^2 + C_1)(\sigma_x^2 + \sigma_y^2 + C_2))$$

Where μ_x and μ_y are the average pixel intensities of the original and reconstructed images, σ_x and σ_y represents their standard deviations, σ_{xy} measures the covariance between corresponding pixels, C_1 and C_2 represents the slight coefficients to evade division by zero.
SSIM provides a more human-centric quality assessment compared to PSNR, which solely focuses on pixel intensity differences. The performance of the proposed EWBS method was compared with traditional wavelet shrinkage denoising models. Table 1 and Table 2 present the average PSNR and SSIM values, respectively, obtained after denoising 120 test images mixed with various noise types at different levels using EWBS and traditional WBS, and then comparing these with their respective original (clean) mammograms. The first column in both tables represents Gaussian and speckle noise mixed at different levels (σ = 10, 20, 30, 40) with the original mammograms. The second column shows the salt-and-pepper noise applied at different probability levels (0.01, 0.02, 0.03, and 0.04). In this experiment, the same 120 noisy test mammograms were also denoised using WBS with universal hard thresholding and WBS with VisuShrink soft thresholding, both implemented using the PyWavelets library in the Anaconda Distribution 2025.06 platform. The average PSNR and SSIM values for these two traditional WBS denoising methods are shown in columns three and four, respectively. These are compared with the PSNR and SSIM values of the proposed WBS method, which are presented in the fifth column of both tables.
PSNR / SSIM averages in each row (both tables) calculated as follows:

- PSNR / SSIM of WBS universal hard threshold = (Sum of PSNR / SSIM of 30 noisy images (10 mammograms * 3 types of noise)) / 30
- PSNR / SSIM of WBS visuShrink soft threshold = (Sum of PSNR / SSIM of 30 noisy images (10 mammograms * 3 types of noise)) / 30
- PSNR / SSIM of proposed EWBS = (Sum of PSNR / SSIM of 30 noisy images (10 mammograms * 3 types of noise)) / 30

These average values are also plotted in the graph shown in Fig. 12, which illustrates the superiority of the proposed approach compared to existing WBS methods. It is evident from the above discussion and the experimental results presented in Tables 1 and 2 that the proposed EWBS method, which integrates K-means clustering with a CNN, outperforms traditional wavelet block shrinkage by approximately 30% in PSNR and 5% in SSIM, as calculated by comparing their respective average values.
We also compared the PSNR and SSIM scores of the proposed EWBS method with several recently researched AI-based denoising approaches, explored by Dabov et al., 2007 [38], Singh et al., 2019 [31], Zhang et al., 2010 [16], and Eckert et al., 2019 [30]. When the EWBS results were evaluated against the outcomes reported by Eckert et al. (2019 [30], we got the corresponding comparative scores as presented in Table 3. The analysis demonstrates that EWBS offers improved performance over both traditional and existing AI-based denoising methods, offering superior performance in preserving mammogram quality and structural integrity.

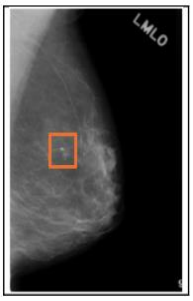

Fig. 13: Original mammogram with mass lesion

Table3: Performance comparison of proposed EWBS against other AI-based denoising methods

Methods	PSNR	SSIM
WBS	25.78	0.89
BM3D [38]	35.49	0.80
Singh [31]	33.50	0.78
DNCNN [16]	36.08	0.84
ResNet [30]	36.18	0.84
EWBS	38.64	0.91

4. Discussions

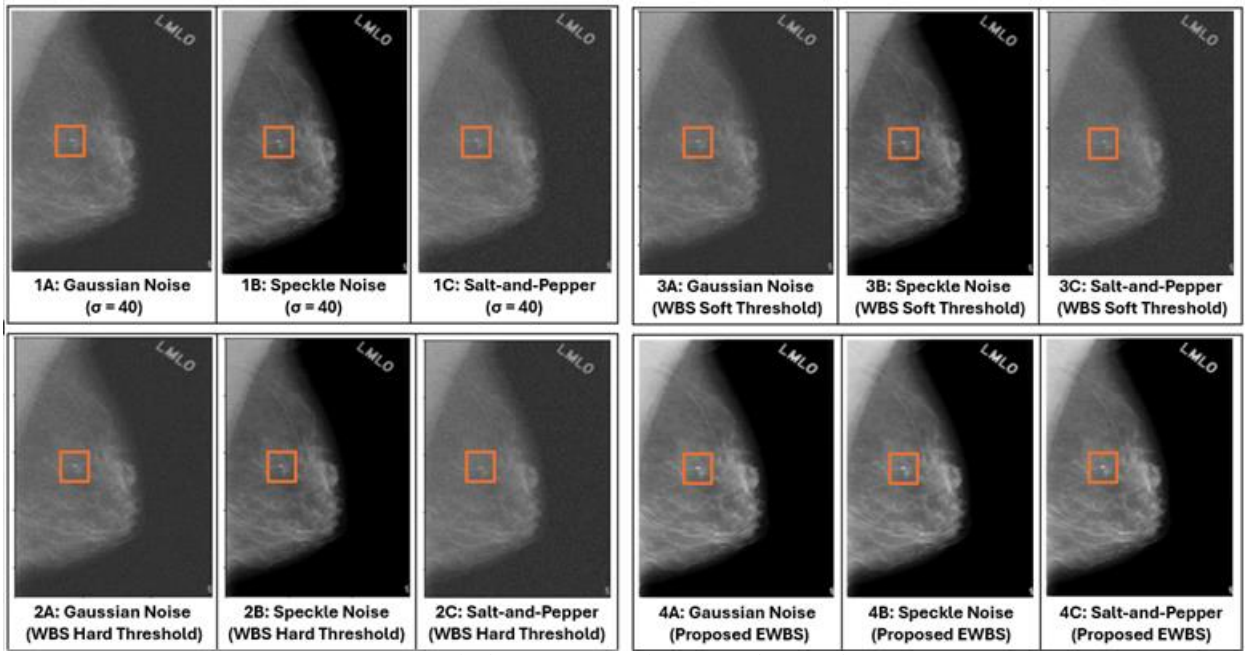

Fig. 14: Denoised Mammograms using WBS and proposed EWBS

Fig. 13 shows an original mammogram from the DDSM mammography library containing a tiny mass lesion highlighted in the orange box. We have carefully chosen this texture to visually illustrate the superiority of EWBS compared to the traditional WBS. The mammogram in Fig. 13 was further mixed with Gaussian noise, Speckle noise, and Salt-and-Pepper noise, each with a standard deviation (σ) of 40, to illustrate how noise impacts the appearance of a subtle but important mass lesion, as shown in segments 1A, 1B, and 1C of Fig. 14. This feature is critical for radiologists to categorize the mammogram as benign, malignant, or negative. Segments 2A, 2B, and 2C of Fig. 14 depict filtered mammograms denoised with the traditional WBS hard thresholding method, and segments 3A, 3B, and 3C depict filtered mammograms denoised with the traditional WBS soft thresholding method. This indicates that although both WBS methods are good at denoising Gaussian noise, they have relatively poor performance for Speckle noise, and especially for Salt-and-Pepper noise, as the white dot in the orange box is not clear in these cases. Segments 4A, 4B, and 4C of Fig. 14 depict filtered mammograms denoised with the proposed EWBS; it is evident that the subtle mass (white dot in the orange box) is prominent in all three segments. Hence, we can conclude that K-Means clustering and the CNN-based shrinkage empower the EWBS to denoise the mammogram by generalizing the shrinkage function across different noise types and noise levels, while keeping important features such as microcalcifications and tissue structures across different regions (e.g., fatty tissue, blood vessels) intact, which is crucial for accurate diagnosis.

5. Conclusion

Our research investigates various types of noise that degrade the visual quality of mammograms, reviews conventional denoising mechanisms, and examines recent advances in subband adaptive denoising methods. We also explore how contemporary research leverages artificial intelligence—particularly CNN—to enhance mammogram denoising. In this study, we propose a novel denoising approach, EWBS, which integrates wavelet transforms, K-Means clustering, and CNNs to efficiently reduce noise while preserving critical diagnostic features. The proposed method outperforms traditional and state-of-the-art techniques, demonstrating significant potential to improve breast cancer screening and diagnosis, thereby contributing to better patient outcomes.

In this experiment, we used mammograms of constant resolution $1800 * 2300$ to keep the computational complexity at an optimum level. The proposed EWBS can be extended to high and varying resolutions. Determining the optimal number of clusters (k) Such scenarios require further exploration, as they directly influence denoising performance and may require extensive parameter tuning, robust cluster validation techniques, and higher computational power. Also, in this experiment, mammograms are decomposed at one level using Symlets or Coiflets families of wavelet bases; further study can be conducted to evaluate the effectiveness of EWBS for multi-level wavelet decomposition with different families of wavelet bases. We observed that the Symlets wavelet function is good at preserving the edges of mammograms, while Coiflets provide good smoothness and asymmetry, potentially beneficial for handling smooth and textured regions in mammograms.

The performance of the CNN-based shrinkage function could be further improved and generalized by training with mammograms from multiple vendors. In our current research, the training data is limited to two vendors (DBA and HOWTEK). Additionally, there is potential to extend the applicability of EWBS to other medical imaging modalities, such as CT and MRI.

Acknowledgement

None.

Declaration

I hereby declare that:
1. This work is original and has not been submitted elsewhere for credit
2. All sources are properly cited
3. No AI-generated content was used without proper verification

Conflict of Interest

No potential conflict of interest relevant to this article was reported.

References

[1] Bray, F., Ferlay, J., Laversanne, M., Soerjomataram, I., Jemal, A., & Torre, L. A. (2024). Global cancer statistics 2022: GLOBOCAN estimates of incidence and mortality worldwide for 36 cancers in 185 countries. CA: A Cancer Journal for Clinicians, 74, 229–263. https://doi.org/10.3322/caac.21834

[2] Kuroishi, T., Hirose, K., Suzuki, T., Tominaga, S., & Takashima, S. (1992). The effect of breast self-examination on early detection and survival. Japanese Journal of Cancer Research, 83, 344–350. https://doi.org/10.1111/j.1349-7006.1992.tb00113.x

[3] Chen, L., Linden, H. M., Anderson, B. O., & Li, C. I. (2014). Trends in 5-year survival rates among breast cancer patients by hormone receptor status and stage. Breast Cancer Research and Treatment, 147, 609–616. https://doi.org/10.1007/s10549-014-3112-6

[4] Aristokli, N., Polycarpou, I., Themistocleous, S. C., Sophocleous, D., & Mamais, I. (2022). Comparison of the diagnostic performance of magnetic resonance imaging (MRI), ultrasound and mammography for detection of breast cancer based on tumor type, breast density and patient's history: A review. Radiography, 28, 848–856. https://doi.org/10.1016/j.radi.2022.01.006

[5] Jung, H., Ryu, S., Kim, S., Kim, J. H., & Kim, J. G. (2019). Effect of digital mammography for breast cancer screening: A comparative study of more than 8 million Korean women. Radiology, 293, 48–54. https://doi.org/10.1148/radiol.2019190951

[6] Warren, L. M., Mackenzie, A., Given-Wilson, R., & Wallis, M. G. (2012). Effect of image quality on calcification detection in digital mammography. Medical Physics, 39, 3202–3213. https://doi.org/10.1118/1.4718571

[7] Huda, W., Ogden, K. M., Scalzetti, E. M., Dance, D. R., & Bertrand, E. A. (2006). How do lesion size and random noise affect detection performance in digital mammography? Academic Radiology, 13, 1355–1366. https://doi.org/10.1016/j.acra.2006.07.011

[8] Iflaq, P., Wilczek, M., Bell, D., et al. (2025). Dead pixel artifact. Radiopaedia. https://doi.org/10.53347/rID-98016

[9] Saunders, R. S., Baker, J. A., Delong, D. M., Johnson, J. P., & Samei, E. (2007). Does image quality matter? Impact of resolution and noise on mammographic task performance. Medical Physics, 34, 3971–3981. https://doi.org/10.1118/1.2776253

[10] Pereira, L., et al. (2021). Biological effects induced by doses of mammographic screening. Physica Medica, 87, 90–98. https://doi.org/10.1016/j.ejmp.2021.06.002

[11] Cahn, R. N., Cederström, B., Danielsson, M., Hall, A., Lundqvist, M., & Nygren, D. (1999). Detective quantum efficiency dependence on x-ray energy weighting in mammography. Medical Physics, 26, 2680–2683. https://doi.org/10.1118/1.598807

[12] da Costa Junior, C. A., & Patrocinio, A. C. (2019). Performance evaluation of denoising techniques applied to mammograms of dense breasts. In XXVI Brazilian Congress on Biomedical Engineering (pp. 369–374). Springer. https://doi.org/10.1007/978-981-13-2119-1_58

[13] Nazir, N., Sarwar, A., & Saini, B. S. (2024). Recent developments in denoising medical images using deep learning: An overview of models, techniques, and challenges. Micron, 180, 103615. https://doi.org/10.1016/j.micron.2024.103615

[14] Cai, T. T., & Silverman, B. W. (2001). Incorporating information on neighboring coefficients into wavelet estimation. Sankhyā: The Indian Journal of Statistics, Series A, 63, 127–148. http://www.jstor.org/stable/25053168

[15] Dewangan, P., & Goswami, R. (2012). Adaptive wavelet thresholding for image denoising using various shrinkage under different noise conditions. International Journal of Engineering Research and Technology, 1(4), 1–5.

[16] Zhang, X., Burger, M., Bresson, X., & Osher, S. (2010). Bregmanized nonlocal regularization for deconvolution and sparse reconstruction. SIAM Journal on Imaging Sciences, 3, 253–276. https://doi.org/10.1137/090746379

[17] Rahman, W. T., & Helvie, M. A. (2022). Breast cancer screening in average and high-risk women. Best Practice & Research Clinical Obstetrics & Gynaecology, 83, 3–14. https://doi.org/10.1016/j.bpobgyn.2021.11.007

[18] Perez, A. M. M. M., Lopes, L. A. S., Caron, R. F., Oliveira, B. B., & Poletti, M. E. (2024). Performance evaluation of six digital mammography systems. Radiation Physics and Chemistry, 218, 111635. https://doi.org/10.1016/j.radphyschem.2024.111635

[19] Kumar, A., Kumar, P., & Srivastava, A. (2022). A skewness reformed complex diffusion based unsharp masking for the restoration and enhancement of poisson noise corrupted mammograms. Biomedical Signal Processing and Control, 73, 103421. https://doi.org/10.1016/j.bspc.2021.103421

[20] Ghazdali, A., Hadri, A., & Laghrib, A. (2024). Poisson noise and Gaussian noise separation through copula theory. Multimedia Tools and Applications, 83, 67927–67952. https://doi.org/10.1007/s11042-023-17898-y

[21] Pashaei, E., & Pashaei, E. (2023). Gaussian quantum arithmetic optimization-based histogram equalization for medical image enhancement. Multimedia Tools and Applications, 82, 34725–34748. https://doi.org/10.1007/s11042-023-15025-5

[22] Cederström, B., Svensson, B., Danielsson, M., & Fredenberg, E. (2014). The influence of anatomical noise on optimal beam quality in mammography. Medical Physics, 41, 071910. https://doi.org/10.1118/1.4900611

[23] Chowdappa, A., & Sheshadri, H. (2018). Probabilistic identification and estimation of noise: Application to MR images. Biomedical and Pharmacology Journal, 11, 2101–2110. https://doi.org/10.13005/bpj/1589

[24] Arias-Castro, E., & Donoho, D. L. (2006). Does median filtering truly preserve edges better than linear filtering? arXiv. https://arxiv.org/abs/math/0612422

[25] Bhateja, V., Misra, M., & Urooj, S. (2020). Non-linear enhancement techniques for mammograms. In Non-linear filters for mammogram enhancement (pp. 137–160). Springer. https://doi.org/10.1007/978-981-15-0442-6_7

[26] Carnahan, M. B., et al. (2023). False-positive and false-negative contrast-enhanced mammograms: Pitfalls and strategies to improve cancer detection. RadioGraphics, 43, e230100. https://doi.org/10.1148/rg.230100

[27] Amiriebrahimabadi, M., Rouhi, Z., & Mansouri, N. (2024). A comprehensive survey of multi-level thresholding segmentation methods for image processing. Archives of Computational Methods in Engineering. https://doi.org/10.1007/s11831-024-10093-8

[28] Mencattini, A., Salmeri, M., Lojacono, R., & Caselli, F. (2006). Mammographic images enhancement and denoising for microcalcification detection using dyadic wavelet processing. In Proceedings of the IEEE instrumentation and measurement technology conference (IMTC) (pp. 49–53). https://doi.org/10.1109/IMTC.2006.328171

[29] Vikhe, P. S., & Thool, V. R. (2019). A wavelet and adaptive threshold-based contrast enhancement of masses in mammograms for visual screening. International Journal of Biomedical Engineering and Technology, 31, 31–53

[30] Eckert, D., Vesal, S., Ritschl, L., Kappler, S., & Maier, A. (2019). Deep learning-based denoising of mammographic images using physics-driven data augmentation. arXiv preprint. https://arxiv.org/abs/1912.05240

[31] Singh, G., Mittal, A., & Aggarwal, N. (2019). Deep convolution neural network based denoiser for mammographic images. In Advances in computing and data sciences (pp. 187–197). Springer. https://doi.org/10.1007/978-981-13-9939-8_16
[32] Ghosh, S. K., Biswas, B., & Ghosh, A. (2020). Restoration of mammograms by using deep convolutional denoising auto-encoders. In Computational intelligence in data mining (pp. 429–440). Springer. https://doi.org/10.1007/978-981-13-8676-3_38
[33] Benhassine, N. E., Boukaache, A., & Boudjehem, D. (2021). Medical image denoising using optimal thresholding of wavelet coefficients with selection of the best decomposition level and mother wavelet. International Journal of Imaging Systems and Technology, 31, 1906–1920. https://doi.org/10.1002/ima.22589
[34] Do, M. N., & Vetterli, M. (2002). Wavelet-based texture retrieval using generalized Gaussian density. IEEE Transactions on Image Processing, 11, 146–158. https://doi.org/10.1109/83.982822
[35] Pizurica, A., & Philips, W. (2006). Estimating the probability of the presence of a signal of interest in multiresolution single- and multiband image denoising. IEEE Transactions on Image Processing, 15, 654–665. https://doi.org/10.1109/TIP.2005.863021
[36] Starck, J., Murtagh, F., & Candes, E. (2008). Wavelets, ridgelets, and curvelets for Poisson noise removal. IEEE Transactions on Image Processing, 17, 1093–1108. https://doi.org/10.1109/TIP.2008.924386
[37] Heath, M., Bowyer, K., Kopans, D., Moore, R., & Kegelmeyer, W. P. (2000). The digital database for screening mammography. In Digital mammography (pp. 212–218). Springer. http://dx.doi.org/10.1007/978-94-011-5318-8_75
[38] Dabov, K., Foi, A., Katkovnik, V., & Egiazarian, K. (2007). Image denoising by sparse 3-D transform-domain collaborative filtering. IEEE Transactions on Image Processing, 16(8), 2080–2095. https://doi.org/10.1109/TIP.2007.901238